Depth-resolved velocimetry of Hagen–Poiseuille and electro-osmotic flow using dynamic phase-contrast microscopy

Michael Esseling,* Frank Holtmann, Mike Woerdemann, and Cornelia Denz

Institute of Applied Physics, Westfälische-Wilhelms-Universität Münster, Corrensstrasse 2/4, 48149 Münster Germany

*Corresponding author: michael.esseling@uni-muenster.de

Received 30 July 2010; accepted 14 September 2010;
posted 21 September 2010 (Doc. ID 132545); published 26 October 2010

We quantitatively investigate the axial imaging properties of dynamic phase-contrast microscopy, with a special focus on typical combinations of tracer particles and magnifications that are used for velocimetry analysis. We show, for the first time, that a dynamic phase-contrast microscope, which is the integration of an all-optical novelty filter in a commercially available inverted microscope, can visualize three-dimensional velocity fields with a significantly reduced optical sectioning depth. The depth of field for dynamic phase-contrast microscopy is extracted from the three-dimensional response function and compared with the respective values for incoherent bright-field illumination. These results are then used to perform a depth-resolved particle image velocimetry analysis of Hagen–Poiseuille as well as electro-osmotically actuated flows in a microchannel. © 2010 Optical Society of America

OCIS codes: 110.0180, 180.4315, 180.6900, 190.7070.

1. Introduction

In many biological experiments, real-time observation of dynamic processes is desired [1,2], especially in applications where a complex flow field is to be analyzed [3,4]. Apart from the conventional bright-field illumination technique, which is ubiquitous in every microscope from toy to research-grade equipment, several other methods exist that can provide real-time, full-field observation and that all serve a special purpose. The Zernike phase contrast has helped to visualize phase differences and, being the first phase-contrast technique, is still a standard mode of illumination in every scientific microscope [5]. Generalized phase contrast has extended the Zernike approach to a unique mapping area of $0 \leq \varphi \leq \pi$ [6]. Dark-field illumination provides sufficient signal-to-noise ratio (SNR) if very small objects are to be investigated [7]; fluorescence illumination can be used to identify specially marked constituents or substances, e.g., in cell biology [8]. If thin optical slices of a sample are desired, confocal microscopy is the technique of choice. The advent of fast disk-scanning microscopes has enabled the application of confocal microscopy to dynamic biological processes [9]. However, a fundamental limit of this technique is still the limited bandwidth of the scanning apparatus, which enforces a choice between high spatial or high temporal resolution [10]. A further restriction of confocal microscopy is imposed by the number of photons that can be collected from each point during the scanning interval [11]. Another technology that is widely applied to biological experiments is digital holography [12]. It can be used to measure cell thicknesses or refractive indices precisely, but at the cost of computational time [13]. Recently, this technology has been tuned to perform at image rates up to several frames per second [14]. However, if higher frame rates are desired, confocal scanning or digital holography are highly limited. Fluorescence illumination, which, in principle, can provide full-field observation at camera-dependent video rates, is often not biocompatible, because the use of artificial tracer beads and dyes may change

0003-6935/10/316030-09$15.00/0

the behavior of organisms in a biological sample [15]. Furthermore, the maximum achievable frame rate is limited by the number of photons that can be detected by the camera during image acquisition. Another important aspect of an imaging technique, especially in the field of microscopic flow field analysis, is the axial imaging response. In macroscopic and mesoscopic particle image velocimetry (PIV) analysis, the illumination is formed to excite only tracer particles from a thin layer of the sample, which directly determines the measurement depth for the analysis. Because this sheetlike illumination is no longer possible in microscopic particle image velocimetry (μPIV), the sample has to be volume illuminated and the measurement depth is determined by the axial imaging properties, especially by the depth of field [16]. A smaller depth of field allows for thinner optical sectioning in depth-resolved measurements of a flow field. A possibility to enable full-field observation at camera-limited frame rates and with a significantly reduced measurement depth is dynamic phase-contrast microscopy (DynPCM). In this contribution, the axial imaging properties of DynPCM are investigated to determine the depth of field, and the results will be used to perform a depth-resolved PIV analysis of static and periodic flows.

2. Dynamic Phase-Contrast Microscopy

The dynamic phase-contrast microscope consists of an all-optical novelty filter [17], which is integrated into a commercial microscope. In the current realization, the novelty filtering effect is based on a photorefractive material, where a reference laser beam, kept constant in intensity and phase, and an information-bearing signal beam interact through the effect of two-beam coupling [18]. In the case of a diffusion-dominated photorefractive material (for example, $BaTiO_3$), the beam coupling reduces to pure amplitude coupling and energy is transferred in the direction of the c axis of the material, from the signal beam to the reference beam. In the case of static images, the information in the signal beam is totally suppressed and the output, which is observed by a CCD camera, remains dark. Any changes, however, in the signal beam are immediately detected by the novelty filter, leading to a bright output for the changed part of the field of view. Because of the fact that the unchanged background stays dark, dynamics are highlighted and can be detected with a high SNR, a very beneficial aspect, e.g., for a biological researcher [19].

After a change in the image information has been detected, the system adapts to this new condition and the output in the signal channel decays exponentially [18]. The time necessary for this adaptation is determined by the characteristic time constant of the photorefractive material and can be tuned by the total light intensity on the crystal from seconds to hundreds of milliseconds for barium titanate [20,21].

As an interferometric technique, DynPCM can be employed to measure phase changes in a range from $0 \le \varphi \le \pi$ [22]. This unambiguous phase measurement range can be extended up to 2π by a simple phase-triggering technique [23]. Using a two-wavelength setup, phase measurements up to several π have been demonstrated. With this phase resolution, it is possible to observe mixing processes of fluids with a very small refractive index difference using DynPCM [24].

Because of these characteristics, suppression of the stationary output and phase sensitivity, DynPCM offers a very high SNR and inherent motion detection for any kind of sample, which makes the so-acquired images well suited for PIV analysis of flow fields that are seeded with tracer particles [25]. PIV requires at least two consecutive images of a seeded flow, which are then divided into subwindows. To determine the displacement of tracer beads in a subwindow, the two-dimensional correlation matrix between subsequent images is calculated, whose maximum defines the average displacement. In general, PIV evaluation only accounts for the two transversal velocity components of the flow in one image plane [two-dimensional, two-component (2D-2C)]. Stereoscopic measurements and subsequent particle tracking can identify all three velocity components in one image plane [26]. For the three-dimensional measurement of constant or periodic flows, the two-dimensional flow field can be extracted for several image planes through optical sectioning [three-dimensional, two-component (3D-2C)]. For depth-resolved measurements in a volume-illuminated sample, the depth of field of the technique must be measured to determine which layers of a flow contribute to the PIV analysis of the acquired data. By applying a simple gray value threshold to the image data, tracer beads that are irrelevant for the analysis are blocked out.

3. Particle-Response Function

Optical sectioning as a technique to obtain depth-resolved images has been known since the beginning of the last century [27]. It exploits the fact that images away from the focal plane get blurred and lose intensity. A prerequisite for the use of optical sectioning in PIV is the limited depth of field of a microscope objective. This figure of merit can be described using the impulse response or point-spread function (PSF) of a lens [28]. A perfect lens would image a δ function in the object plane directly to a corresponding δ peak in the image plane. A real lens, however, is limited by diffraction at the aperture. To investigate the depth of field, one must examine the intensity distribution along the optical axis [28]

$$I(u) = I_0 \frac{\sin(\frac{u}{4})}{\frac{u}{4}}, \tag{1}$$

where $u = \frac{2\pi}{\lambda}(\frac{a}{f})^2 z$ is the dimensionless axial distance from the focal plane, a and f are the aperture and focal length of the lens, λ is the wavelength, and I_0 is the central intensity in the geometric focus at $u = 0$. When the central intensity has dropped to

80% of its maximum value, the image is regarded as out of focus [28]. This is the case at

$$\Delta z = \pm \frac{3.2\lambda}{2\pi}\left(\frac{f}{a}\right)^2 \approx \pm \frac{\lambda}{2}\left(\frac{f}{a}\right)^2. \quad (2)$$

Furthermore, for a microscope objective the approximation $n \cdot \frac{a}{f} \approx \mathrm{NA}$ holds [29]. Replacing the wavelength in the medium by the vacuum wavelength $\lambda_0 = \lambda \cdot n$, the total depth of field can be written as

$$\delta_z = 2\Delta z \approx \frac{n\lambda_0}{\mathrm{NA}^2}. \quad (3)$$

The above derivation of the depth of field is based on a perfect, infinitesimal point source [28]. This case is approximated by the use of self-luminous, fluorescent tracer particles that are significantly smaller than the diffraction-limited resolution of the microscope objective. As the typical tracer particles used for the technique of DynPCM are larger than the diffraction limit, we introduce the particle-response function (PRF) as the counterpart to the PSF for the case of DynPCM.

4. Measurement of the Particle-Response Function

The experimental setup for measurement of the PRF is depicted in Fig. 1. For DynPCM, the novelty filtering setup is integrated into a commercially available inverted microscope (Nikon Eclipse TE2000-U). The beam of a frequency-doubled Nd:YAG laser ($\lambda = 532\,\mathrm{nm}$) is split up into reference and signal beams, which overlap in a photorefractive crystal. The illumination beam is spatially filtered for homogeneous illumination and coupled into the microscope. The signal from the camera port is imaged onto a CCD camera by a 100 mm lens. As for the positioning of the photorefractive $BaTiO_3$ crystal, a position shortly behind the Fourier plane is a reasonable trade-off between uniform grating formation times for all spatial frequencies and minimum disturbances from imperfections in the crystal. The polarization of the beams is adjusted to be extraordinary due to the significantly higher electro-optic coefficient and beam coupling constant in this geometry [30].

For determination of the PRF in different magnifications, 0.01 vol.% dilutions of polystyrene tracer beads are placed on a microscope slide with a coverslip. Images of one tracer particle are recorded at different positions symmetrically around the focal plane. A transversal profile through the center of the particle in each height is made, and these cuts are stacked to form the three-dimensional PRF. It is sufficient to investigate one transverse dimension because the particles are spherical and the imaging properties of the dynamic phase-contrast microscope are cylinder symmetrical, hence the x and y cuts are interchangeable. To measure the depth of field, a so-called z cut is made through the center of the PRF in the axial direction. The z cut shows the particle central intensity against the defocusation and can be used to determine at which axial position the intensity has decreased to 80% of its maximum value (Fig. 2).

Scanning in the axial direction is done with a stepper motor with a minimum resolution of 32 nm. In the case of the Nikon TE2000, the objective turret is moved relative to the sample, which is valid,

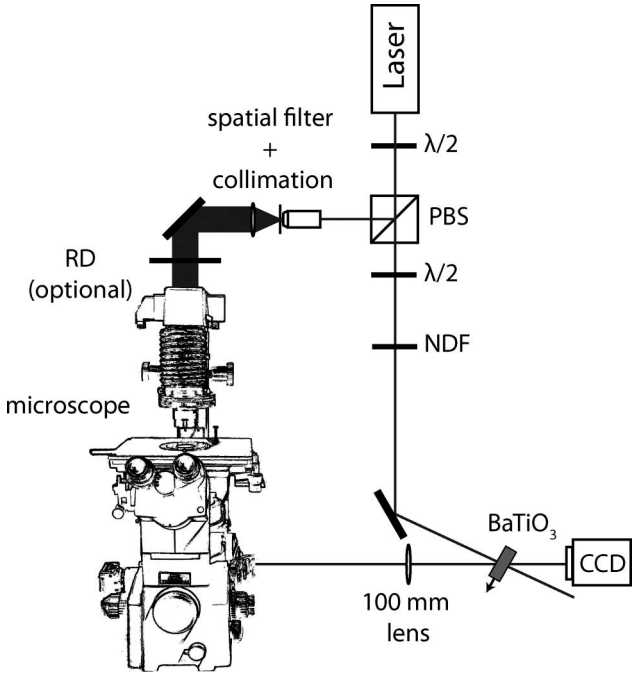

Fig. 1. Experimental setup for measurement of the PRF.

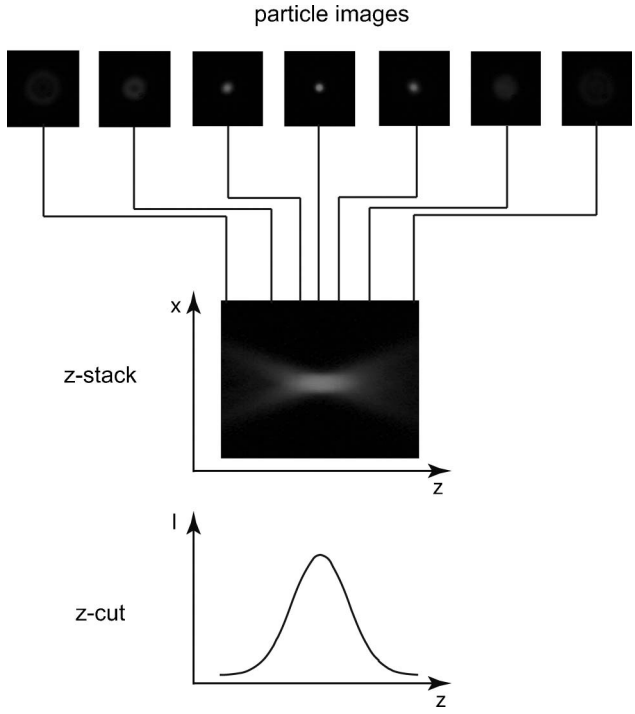

Fig. 2. Schematic workflow for composition of the z stack and z cut from fluorescent particle images.

because all the used microscope objectives are infinity corrected. Because of the inherent novelty filtering of DynPCM, the tracer particles have to be kept under constant lateral motion during image acquisition; otherwise, the image information would be suppressed as static. This is accomplished through the use of a motorized lateral scanning sample holder on top of the microscope stage. In order to obtain valid measurements for the depth of field, it is checked before each measurement that the tracer bead under investigation sticks to the glass slide and does not move in the axial direction.

For comparison of the depth of field of DynPCM with the respective value for incoherent bright-field illumination, the illumination paths in both cases must coincide exactly because small deviations can change the shape of the z cut and make a direct comparison impossible. Therefore, incoherent bright-field illumination is simulated by the same laser that is used for DynPCM image acquisition. Its coherence is effectively destroyed by a rotating diffuser (RD) that is added after spatially filtering the beam.

5. Axial Imaging Response

Results for the measurements of the PRF and the extracted z cuts (Figs. 3–5) show that there is a qualitative difference between incoherent illumination and DynPCM. In the first case, the response function is asymmetric around the focal plane, which can be explained by the higher refractive index of the polystyrene sphere with respect to the surrounding medium. Therefore, light is scattered by the particle, resulting in a darker image if the particle is below the focal plane. Because the sphere acts as a lens, the light is refocused when the particle is above the focal plane. In contrast to this behavior, DynPCM shows a symmetric response for the PRF and depth of field for all combinations of magnifications and tracer particles with the maximum intensity near the focal plane at $z = 0\,\mu$m. In PIV evaluation, this allows us to define an intensity threshold to determine the relevance of tracer particle images and to block out any out-of-focus particles. The symmetric behavior is noteworthy because the dynamic phase contrast, as was pointed out before, is responding to phase and amplitude changes alike, so the asymmetric intensity profile [Fig. 3(b)] could result in a similar DynPCM profile. However, in this case, as was pointed out before, the light is focused by the polystyrene sphere, whereas the illumination light that does not pass the bead can be regarded as a plane wave. The Gouy phase shift that originates from this focusing with respect to the illumination wave creates the symmetric signal due to the fact that the

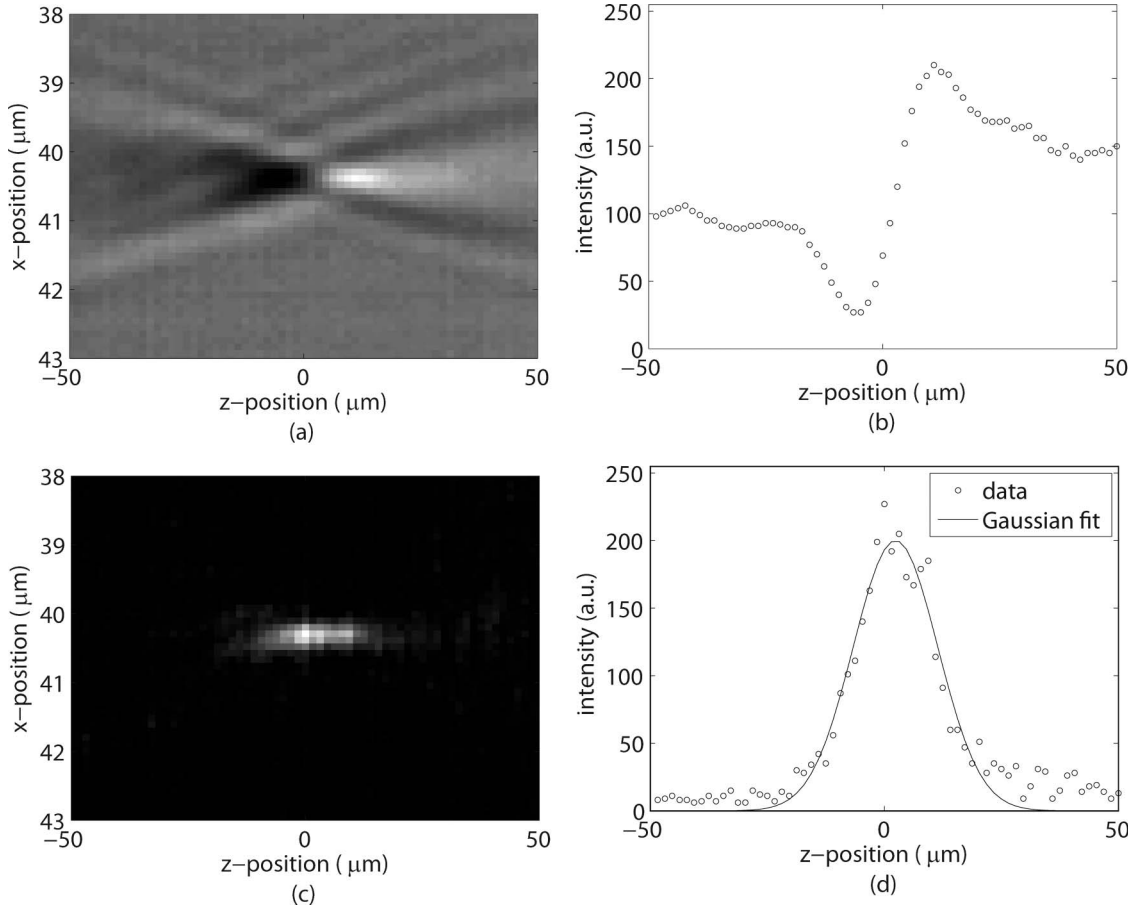

Fig. 3. PRF and z cut of dynamic phase-contrast setup with incoherent illumination (a) and (b) and in DynPCM mode [(c) and (d)]: magnification, 10×; NA, 0.25; and particle size, 1 μm.

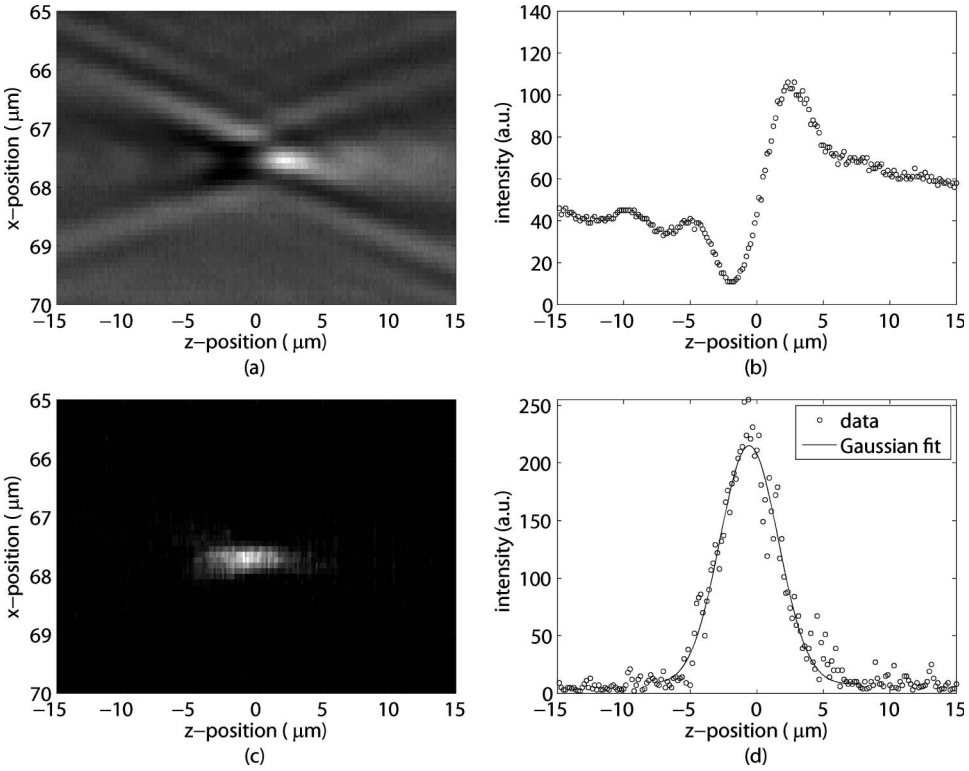

Fig. 4. Particle-response function and z cut of dynamic phase-contrast setup with incoherent illumination (a) and (b) and in DynPCM mode [(c) and (d)]: magnification, 20×; NA, 0.45; and particle size $1\,\mu$m.

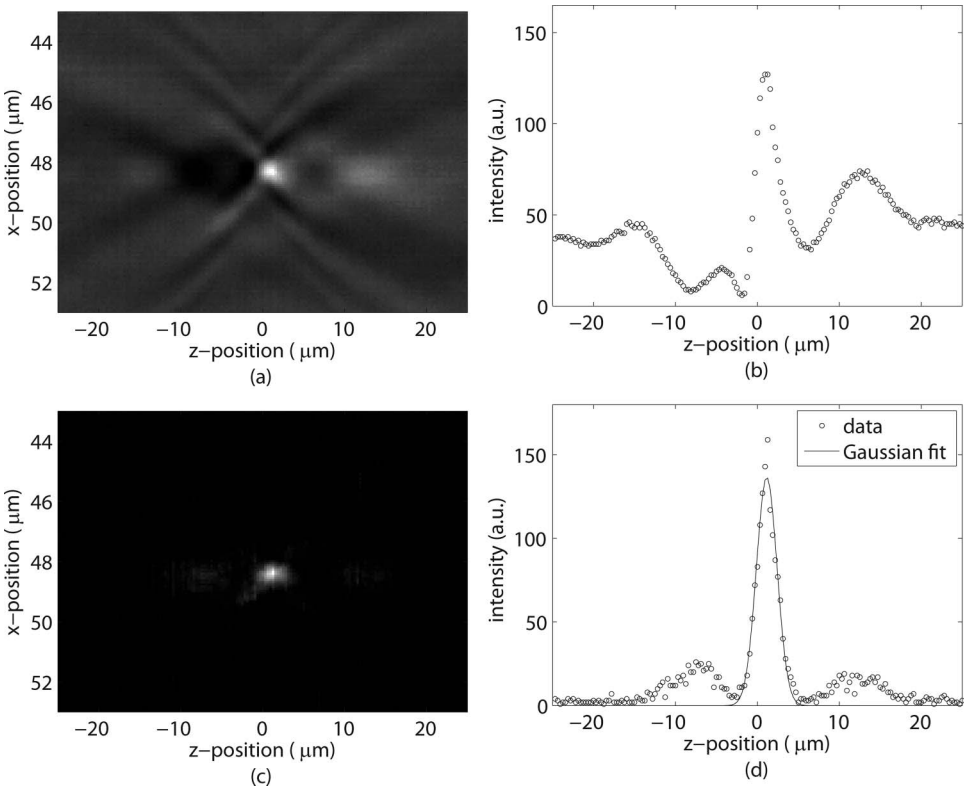

Fig. 5. Particle-response function and z cut of dynamic phase-contrast setup with incoherent illumination (a) and (b) and in DynPCM mode [(c) and (d)]: magnification, 60×; NA, 0.70; and particle size $0.725\,\mu$m.

Table 1. Depth of Field and Signal-to-Noise Ratio for Incoherent Illumination and DynPCM

Magnif./NA	d_p (μm)	$\delta_{z,\text{incoh.}}$ (μm)	$\delta_{z,\text{DynPCM}}$ (μm)	+/− (%)	$\text{SNR}_{\text{incoh.}}$	$\text{SNR}_{\text{DynPCM}}$
10 × /0.25	1	15.5	12.1	−22	1.9	13.7
20 × /0.45	1	3.3	2.9	−12	2.3	10.0
60 × /0.70	0.725	1.9	1.7	−11	3.2	22.2

phase transfer function of DynPCM is symmetric [22]. Given that the sphere acts as a ball lens and focuses a plane wave of the diameter of the sphere, the Rayleigh length of the focused beam can be approximated with $z_0 \approx 78$ nm. Even considering spherical aberrations that may deteriorate the focus size, this perfectly satisfies the condition of being sufficiently smaller than the resolution limit and therefore being an infinitely small point source for the Gouy phase shift. This *phase point* is detected with DynPCM and follows Eq. (2). For a magnification of 60× with a tracer bead size of 725 nm, it is even possible to resolve the first sidelobes of the theoretically predicted sinc^2 shape for the depth of field.

It should be noted that, for incoherent illumination, there is a parasitic modulation of the z cut in 20× and 60×. After replacing the RD illumination by the incandescent microscope illumination, the modulation still remains. The position and distance between the maxima of this higher frequency modulation are independent of the tracer size but only depend on the position of the correction ring of the microscope objectives. This leads to the conclusion that it originates from scattered light inside the microscope objectives. Because the Nikon TE2000 is an inverted microscope, special objectives have to be used with a correction ring that allows the adjustment to different thicknesses of cover slides between objective and sample. In any case, the modulations are not present in the DynPCM images.

For comparison of the respective depths of field, which will later determine the PIV measurement depth, a Gaussian fit was applied to the DynPCM response to determine the drop to 80%. For the case of incoherent illumination, the respective values were extracted manually. From the data in Table 1, it can be concluded that DynPCM has a significantly reduced PIV measurement depth as compared to bright-field illumination. The reduction in δ_z can be as high as 22%, which allows for thinner optical sectioning in depth-resolved PIV analysis. Additionally, the SNR is greatly improved because the image background is suppressed by DynPCM. The ideal case of a totally suppressed background is not achieved in this case because vibrations from the moving microscope sample holder introduce additional marginal phase deviations to the background signal.

6. Depth-Resolved Particle Image Velocimetry Measurements

The previously measured depth of field gives an estimate of the smallest possible axial separation between cross sections in PIV analysis. To demonstrate the feasibility of DynPCM as a PIV image acquisition device, two qualitatively completely different flow scenarios are analyzed: a pressure-driven flow, also called the Hagen–Poiseuille flow, around a corner and an electro-osmotically actuated flow in a poly(dimethylsiloxane) (PDMS) microchannel. Both flows are recorded with a camera at 48 frames/s, which is sufficient to resolve the movement of tracer particles. The existing camera, though, can easily be replaced by a faster model, allowing even higher acquisition speeds.

A. Hagen–Poiseuille Flow

The first measurement is performed in a capillary electrophoresis (CE) microchannel (width/height: 50/20 μm) where a seeded flow (tracer size: 725 nm) is driven by different filling heights in the reservoirs of the channel. The PIV evaluation is done in the T mixing area (see Fig. 6), where both straight flow and flow around a corner exist. Placed in the mixing area is an obstruction, which is stationary and thus should not appear in the dynamic phase-contrast images.

Ten cross sections with an axial separation distance of 2 μm are recorded, beginning near the bottom of the channel. This spacing is larger than the previously measured depth of field of the 60× microscope objective. The larger spacing enables a lower threshold for preprocessing the acquired images and thus a higher remaining particle density in the images. The tracer initial concentration in the liquid is also crucial: too many particles lead to uncontrolled speckles due to the coherent illumination in DynPCM, and too few particles lead to high error rates in determination of the flow field because the correlation of only a few tracer particles can be ambiguous. A concentration of 1 vol.% of tracer beads has proved to be a good compromise.

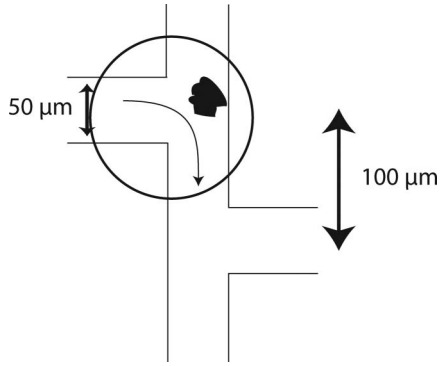

Fig. 6. Basic layout of electrophoresis microchannel and measurement area (circle) with obstruction.

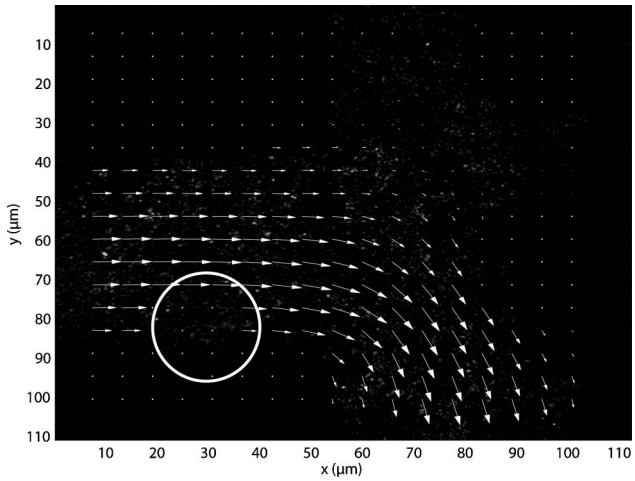

Fig. 7. Flow profile inside the CE microchannel at $z = 10\,\mu$m; note the erroneous area in the circle, where the PIV algorithm was unable to determine valid velocity vectors.

Figure 7 shows the image data of the cross section at $z = 10\,\mu$m, overlaid with the calculated PIV displacement. The PIV analysis is done using the correlation method of the mPIV Toolbox [31] in a 128×128 pixel subwindow (corresponding to a real space size of $14.35\,\mu\text{m} \times 14.35\,\mu\text{m}$) and correction of spurious vectors. For a higher fraction of valid vectors, the algorithm has been adjusted to average the displacement information of 50 images in the correlation plane [16]. Stacking all ten evaluated cross sections, one obtains the 3D-2C flow field (Fig. 8). In the resulting images of the T junction, DynPCM suppresses the borders of the channel as well as the obstruction in the vicinity of the T junction. The parabolic velocity profile that is expected from the fluid dynamic theory for the Hagen–Poiseuille flow [32] is clearly visible in the transversal (Fig. 7) as well as in the axial direction (Fig. 8). However, the algorithm had a problem identifying the correct velocity in a certain region (circle in Fig. 7). One could argue that this is purely accidental, but the same error occurs in this particular region in all ten cross sections (Fig. 8). Because no irregularities can be identified in the DynPCM raw data, the reason for this error is most likely connected to the PIV algorithm or its modification to the correlation average technique, respectively. Furthermore, it blocks out displacement vectors with an insufficient SNR in the correlation plane, which also decreases the number of valid vectors.

B. Electro-Osmotic Flow

The second PIV measurement is aimed at the velocity profile of the electro-osmotic flow (EOF) in a PDMS microchannel. Electro-osmotic flow is a different way to actuate a flow using an external electric field. For the resulting velocity profile, theory predicts a pluglike shape with a large area of uniform motion [32,33]. Because the transported fluid volume is proportional to the cross section of the microchannel, EOF scales well in microfluidic applications. To observe EOF, microfluidic half-channels (width/height: $300/50\,\mu$m) are fabricated by PDMS replica molding [34,35]. Together with a glass slide as the bottom layer, they form a full channel: pipet tips are added as additional flow reservoirs, and copper wires are inserted into these reservoirs as electrodes.

The channel is filled with $1\,\mu$m tracer beads in a 1 vol.% dilution. It is important that the channel reservoirs are filled to the same height, otherwise the resulting pressure difference will induce a Hagen–Poiseuille flow, which is detrimental for the observation of EOF. Images are acquired with the 20× microscope objective at different heights in the channel. The resulting velocity at the starting cross section at $5.3\,\mu$m (Fig. 9) shows that the theoretical prediction of a pluglike shape is true in the transverse direction. For a homogeneous flow profile, one can calculate the mean velocity v_{mean} in the channel and compare it for different heights (see Fig. 10). The result confirms the theoretical assumption of

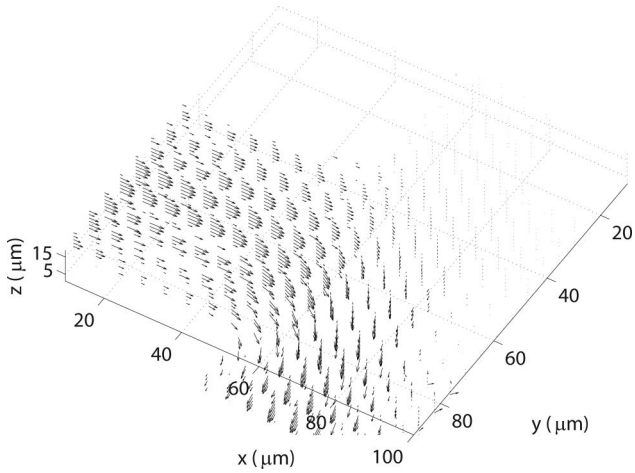

Fig. 8. Depth-resolved velocity profile of the flow in the CE microchannel: axial separation between velocity errors, $2\,\mu$m.

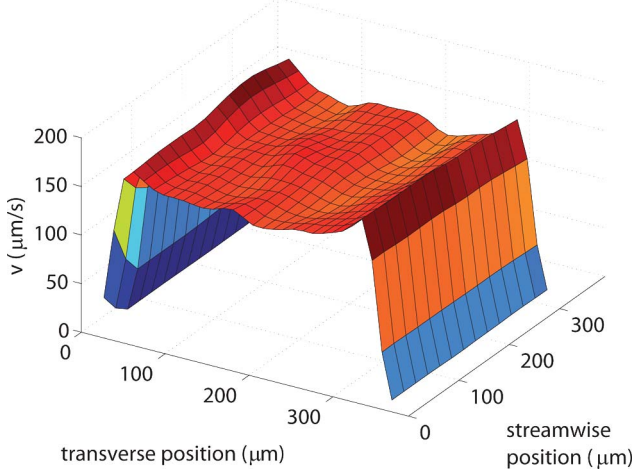

Fig. 9. (Color online) Velocity profile of the EOF at a distance of $5.3\,\mu$m from the bottom of the channel.

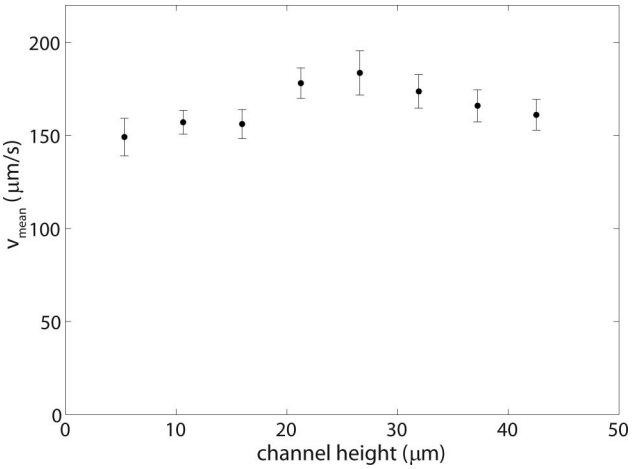

Fig. 10. Mean velocity in the electro-osmosis channel at different heights; error bars indicate standard deviation.

a pluglike shape in both the transversal and the axial directions.

7. Conclusion

We have quantitatively investigated the three-dimensional PRF of DynPCM for several experimental configurations that are applied in the field of PIV analysis. The depth of field has been extracted from the PRF and compared for two different imaging techniques. It could be shown that DynPCM offers reduced PIV measurement depth, a response function that is symmetric about the focal plane, and a significantly enhanced SNR for any kind of tracer particle due to the inherent background suppression. The results for the depth of field give a reliable estimate for the axial separation of cross sections in a depth-resolved flow analysis. For the first time, 3D-2C PIV measurements with a separation as low as 2 μm are demonstrated using DynPCM. Furthermore, DynPCM was utilized to perform a full-field PIV analysis of the EOF in a PDMS microchannel. The theoretical predictions of a pluglike velocity profile are confirmed. The next consequent step would be the application of DynPCM to three-dimensional biological flows, where the technique benefits from its biocompatibility due to the fact that the system, in principle, also works with nonartificial biocompatible tracer particles (such as yeast or milk) and requires only low light powers.

Financial support from the European Union (EU) within the framework of *Photonics4Life*, the Deutsche Forschungsgemeinschaft within the framework of the priority program SPP 1147, and the German–Chinese Transregional Research Project TRR61 is gratefully acknowledged.

References

1. B. Kemper, D. Carl, J. Schnekenburger, I. Bredebusch, M. Schaefer, W. Domschke, and G. von Bally, "Investigation of living pancreas tumor cells by digital holographic microscopy," J. Biomed. Opt. **11**, 034005 (2006).
2. P. Prasad, *Introduction to Biophotonics* (Wiley-Interscience, 2003).
3. B. E. Zima-Kulisiewicz and A. Delgado, "Synergetic microorganismic convection generated by *Opercularia asymmetrica* ciliates living in a colony as effective fluid transport on the micro-scale," J. Biomech. **42**, 2255–2262 (2009).
4. S. T. Wereley and C. D. Meinhart, "Recent advances in microparticle image velocimetry," Annu. Rev. Fluid Mech. **42**, 557–576 (2010).
5. F. Zernike, "How I discovered phase contrast," Science **121**, 345–349 (1955).
6. J. Gluckstad, "Phase contrast image synthesis," Opt. Commun. **130**, 225–230 (1996).
7. T. Horio and H. Hotani, "Visualization of the dynamic instability of individual microtubules by dark-field microscopy," Nature **321**, 605–607 (1986).
8. J. W. Taraskaz and W. N. Zagotta, "Fluorescence applications in molecular neurobiology," Neuron **66**, 170–189 (2010).
9. P. Houpt and A. Draaijer, *A Real-Time Confocal Scanning Microscope for Fluorescence and Reflection*, Institute of Physics Conference Series (Institute of Physics, 1990), pp. 639–642.
10. J. B. Pawley, ed., *Handbook of Biological Confocal Microscopy* (Springer, 2006).
11. E. Wang, C. Babbey, and K. Dunn, "Performance comparison between the high-speed Yokogawa spinning disc confocal system and single-point scanning confocal systems," J. Microsc. Oxford **218**, 148–159 (2005).
12. B. Kemper and G. von Bally, "Digital holographic microscopy for live cell applications and technical inspection," Appl. Opt. **47**, A52–A61 (2008).
13. J. Garcia-Sucerquia, W. Xu, S. Jericho, P. Klages, M. Jericho, and H. Kreuzer, "Digital in-line holographic microscopy," Appl. Opt. **45**, 836–850 (2006).
14. F. C. Cheong, B. Sun, R. Dreyfus, J. Amato-Grill, K. Xiao, L. Dixon, and D. G. Grier, "Flow visualization and flow cytometry with holographic video microscopy," Opt. Express **17**, 13071–13079 (2009).
15. W. Kowalczyk, B. Zima, and A. Delgado, "A biological seeding particle approach for μ-PIV measurements of a fluid flow provoked by microorganisms," Exp. Fluids **43**, 147–150 (2007).
16. C. Meinhart, S. Wereley, and M. Gray, "Volume illumination for two-dimensional particle image velocimetry," Meas. Sci. Technol. **11**, 809–814 (2000).
17. D. Anderson, D. Lininger, and J. Feinberg, "Optical tracking novelty filter," Opt. Lett. **12**, 123–125 (1987).
18. P. Yeh, *Introduction to Photorefractive Nonlinear Optics* (Wiley-Interscience, 1993).
19. R. Cudney, R. Pierce, and J. Feinberg, "The transient detection microscope," Nature **332**, 424–426 (1988).
20. P. Yeh, "Fundamental limit of the speed of photorefractive effect and its impact on device applications and material research," Appl. Opt. **26**, 602–604 (1987).
21. M. Woerdemann, F. Holtmann, and C. Denz, "Full-field particle velocimetry with a photorefractive optical novelty filter," Appl. Phys. Lett. **93**, 021108 (2008).
22. V. Krishnamachari and C. Denz, "Real-time phase measurement with a photorefractive novelty filter microscope," J. Opt. A: Pure Appl. Opt. **5**, S239–S243 (2003).
23. V. Krishnamachari and C. Denz, "A phase-triggering technique to extend the phase-measurement range of a photorefractive novelty filter microscope," Appl. Phys. B **79**, 497–501 (2004).
24. F. Holtmann, M. Eversloh, and C. Denz, "Label-free analysis of microfluidic mixing processes by dynamic phase contrast microscopy," J. Opt. A: Pure Appl. Opt. **11**, 034014 (2009).

25. C. Willert and M. Gharib, "Digital particle image velocimetry," Exp. Fluids **10**, 181–193 (1991).
26. F. Holtmann, M. Oevermann, and C. Denz, "Dynamic phase-contrast stereoscopy for microflow velocimetry," Appl. Phys. B **95**, 633–636 (2009).
27. F. Lucas, "The architecture of living cells—recent advances in methods of biological research—optical sectioning with the ultra-violet microscope," Proc. Natl. Acad. Sci. USA **16**, 599–607 (1930).
28. M. Born and E. Wolf, *Principles of Optics* (Cambridge University Press, 1999).
29. S. Inoué and K. Spring, *Video Microscopy: the Fundamentals* (Plenum, 1997).
30. M. Klein and R. Schwartz, "Photorefractive effects in $BaTiO_3$: microscopic origins," J. Opt. Soc. Am. B **3**, 293–305 (1986).
31. N. Mori and K.-A. Chang, "mPIV-MATLAB PIV Toolbox."
32. N. Nguyen and S. Wereley, *Fundamentals and Applications of Microfluidics* (Artech House, 2006).
33. R. F. Probstein, *Physicochemical Hydrodynamics* (Wiley, 1994).
34. Y. Xia and G. Whitesides, "Soft lithography," Annu. Rev. Mater. Sci. **28**, 153–184 (1998).
35. D. Duffy, J. McDonald, O. Schueller, and G. Whitesides, "Rapid prototyping of microfluidic systems in poly(dimethylsiloxane)," Anal. Chem. **70**, 4974–4984 (1998).